Talbot carpet at the transverse plane produced in the diffraction of plane wave from amplitude radial gratings

SAIFOLLAH RASOULI[1,2,*], ALI MOHAMMAD KHAZAEI[1], AND DAVUD HEBRI [1]

[1] Department of Physics, Institute for Advanced Studies in Basic Sciences (IASBS), Zanjan 45137-66731, Iran
[2] Optics Research Center, Institute for Advanced Studies in Basic Sciences (IASBS), Zanjan 45137-66731, Iran
[*] Corresponding author: rasouli@iasbs.ac.ir

Compiled October 25, 2017

We experimentally demonstrate and theoretically predict a new and unprecedented optical carpet that included all the geometric shadow, and far-field and near-field diffraction patterns at the transverse plane in the diffraction from a radial grating illuminated by a plane wave-front. The main feature of using radial grating is the continuous change of spatial period along the radial direction. Therefore, the geometric shadow, and the near-field and far-field diffraction regimes are mixed at various propagation distances and the traditional definitions for the different diffraction regimes would not apply here. We show that for a given propagation distance, at a certain radial distance the shadow regime changes to the near-field regime and at another certain radial distance the diffraction pattern changes from a near-field to a far-field case.

OCIS codes: (050.0050) Diffraction and gratings; (070.6760) Talbot and self-imaging effects; (260.6042) Singular optics, topological defects.

http://dx.doi.org/10.1364/ao.XX.XXXXXX

1. INTRODUCTION

In the passing a light beam wave-front through a transmission structure such as a grating, three different behaviours can be observed at various propagation distances. At very close distances to the structure the geometric shadow is observed. By increasing propagation distance, first near-field then far-field diffraction patterns are produced. For a given propagation distance, by decreasing the structure dimension, both near-field and far-field regimes get close to the structure plane. Far-field diffraction pattern determines spatial spectrum of the structure and its angular form remains stable at different distances from the structure. Unlike the geometric shadow and far-field diffraction pattern, the near-field diffraction pattern sharply changes by propagation distance. One of the fantastic diffraction phenomenon which was firstly introduced in the near-field diffraction frame, is the Talbot effect or self-imaging. That appears in the illuminating a periodic structure by a spatial coherent light beam in which self-images of the structure replicates at certain imaging planes without the need for a lens [1, 2]. It was used later in the geometric shadow and far-field diffraction frames too [3, 4].

The Talbot effect has found numerous applications in the optical domain, such as in wave-front sensing [5, 6], turbulence characterization [7, 8], phase locking of laser arrays [9], and many others [10]. Nowadays, the concept of the Talbot effect is applied in various wave physics studies including nonlinear dynamics [11], atomic and electron beams [3, 12, 13], x-ray imaging [14], plasmonics [15], exciton-polariton condensates [16], spin waves [17], quantum mechanics [18] and quantum Talbot effect [19], laser physics [20], waveguide arrays [21], matter waves [22, 23], matter-wave interactions [24], and antimatters [25].

In the near-field diffraction from a grating, the intensity pattern over a plane includes propagation axis and grating vector which is called Talbot carpet [26, 27]. All aspects of Talbot effect such as formation of self- and sub-images respectively at the Talbot and fractional Talbot distances appear on the Talbot carpet. A report on the realization of the conventional Talbot carpets over the longitudinal planes has been presented in [27].

We have recently proposed a comprehensive and rigorous mathematical approach for the treatment of self-imaging [28]. The work consists a detailed analytical and numerical studies of Fresnel images of a considerable number of 1D periodic structures lying in between neighboring self-images (exact self-images and images laterally shifted by half a period). It is shown that by an appropriate designing of the transmission profile of a grating, it is possible to enhance the contrast value of the Talbot self-images namely at the quarter-Talbot distances.

Here for the first time, we demonstrate theoretically and experimentally the formation of Talbot carpet at the transverse planes, consisting all the geometric shadow and the near-field and far-field diffraction patterns in the propagation of a plane wave from a radial grating. We present a detail theoretical calculation by the aid of Fresnel–Kirchhoff integral, for the diffraction from an amplitude radial grating having sinusoidal and binary

profiles. Also diffraction patterns are simulated by the aid of free-space transfer function and experimental work is done with a very simple setup. The results of all three ways of the study are consistent. We observe unprecedented patterns along the radial direction at the transverse planes. Theoretical calculation is done in the polar coordinates.

Here, due to the continuous change of spatial period along the radial direction, three geometric shadow, near-field and far-field diffraction regimes are mixed at various propagation distances and the traditional definitions for the different diffraction regimes are violated. We show that unlike the diffraction from conventional gratings, here general shape of the diffraction patterns does not change by the propagation of the beam.

At a given propagation distance, over the transverse plane the geometric shadow, the near-field, and far-field diffraction patterns are formed at large, intermediate and small radial distances, respectively. This feature raised by the continuous change of the spatial period of the structure along radial direction. For a given propagation distance, we determine conditions for the transitions from the geometric shadow to the near-field and from the near-field to far-field diffraction regions and predict which patterns would be seen at which distances.

It is worth mentioning that, self-imaging of conventional linear gratings has already been investigated in the polar coordinates [29]. Also, a spatial evolution of a Gaussian beam diffracted by an out-of-center sector of a radial grating has been previously reported [30, 31]. But to the best of our knowledge, the general case of diffraction from radial gratings has not been considered in the literature so far.

2. DIFFRACTION FROM 2D STRUCTURES SEPARABLE IN THE POLAR COORDINATES

Here, theory of the diffraction from 2D structures separable in the polar coordinates is presented. Assume $f(x',y')$ as complex amplitude of the light field immediately after the structure, $(z=0)$, and $g(x,y)$ as the resulted complex amplitude at distance z from the structure, by using Fresnel–Kirchhoff diffraction integral [32], we have

$$g(x,y) = h_0 \int_{-\infty}^{\infty}\int_{-\infty}^{\infty} f(x',y') e^{i\alpha[(x-x')^2+(y-y')^2]} dx'dy', \tag{1}$$

where $h_0 = \frac{1}{iz\lambda}\exp(ikz)$ and $\alpha = \frac{\pi}{z\lambda}$, in which λ is the wavelength of the light beam and $k = \frac{2\pi}{\lambda}$ is the wave-number. In the polar coordinates equation 1 gets following form

$$g(r,\theta) = h_0 e^{i\alpha r^2}\int_0^{\infty}\int_0^{2\pi} r'dr'd\theta' f(r',\theta') e^{i\alpha r'^2} e^{-2i\alpha r r'\cos(\theta'-\theta)}, \tag{2}$$

where (r',θ') and (r,θ) are the polar coordinates at input and output planes, respectively (see Fig. 1) . For a 2D structure separable in the polar coordinates system at $z=0$, we get

$$f(r',\theta') = f_R(r') f_\Theta(\theta'). \tag{3}$$

Now, equation 2 can be written in the following form

$$g(r,\theta) = h_0 e^{i\alpha r^2}\int_0^{+\infty} r'dr' f_R(r') e^{i\alpha r'^2}\int_0^{2\pi} d\theta' f_\Theta(\theta') e^{-2i\alpha r r'\cos(\theta'-\theta)}. \tag{4}$$

Here, by using the Jacobi–Anger expansion [33], we have

$$e^{-2i\alpha r r'\cos(\theta'-\theta)} = \sum_{n=-\infty}^{+\infty} (-i)^n J_n(2\pi\rho r') e^{-in(\theta'-\theta)}, \tag{5}$$

where i is the imaginary unit and J_n is the n-th Bessel function of the first kind [33]. As $f_\Theta(\theta')$ is inherently a periodic function with the period 2π, then it can be expanded by using Fourier series as

$$f_\Theta(\theta') = \sum_{m=-\infty}^{+\infty} c_m e^{im\theta'}, \tag{6}$$

where c_m is mth Fourier series coefficient. By replacing equations 5 and 6 in equation 4 and using Hankel transform of order n of the function $f(r)$ [34]

$$\mathcal{H}_n\{f(r)\} = 2\pi\int_0^{+\infty} f(r) J_n(2\pi\rho r) r dr, \tag{7}$$

we get

$$g(r,\theta) = h_0 e^{i\alpha r^2}\sum_{n=-\infty}^{+\infty} c_n (-i)^n e^{in\theta}\mathcal{H}_n\{f_R(r) e^{i\alpha r^2}\}, \tag{8}$$

where $\rho = \frac{r}{\lambda z}$, and we used following identity

$$\int_0^{2\pi} \mathrm{e}^{i(m-n)\theta'}\, d\theta' = 2\pi\delta_{m,n}, \tag{9}$$

in which $\delta_{m,n}$ is the Kronecker delta.

Equation 8 presents the diffraction from 2D structures separable in the polar coordinates.

3. DIFFRACTION FROM RADIAL STRUCTURES

Here, as an important subset of 2D structures separable in the polar coordinates, we define and consider radial structures. We call a 2D structure as a radial structure, when in its transmission function there is not radial dependency. Therefore, a radial structure is a 2D structure separable in the polar coordinates, defined by equation 3, with $f_R(r)=1$. Now, diffraction pattern of a radial structure by considering $f_R(r)=1$ in equation 8, can be written as

$$g(r,\theta) = h_0 e^{i\alpha r^2}\times \left\{c_0\mathcal{H}_0\{e^{i\alpha r^2}\} + \textstyle\sum_{n=1}^{+\infty}(c_n e^{in\theta} + c_{-n}e^{-in\theta})(-i)^n\mathcal{H}_n\{e^{i\alpha r^2}\}\right\}, \tag{10}$$

where we used the following identity

$$\mathcal{H}_{-n}\{f(r)\} = (-1)^n\mathcal{H}_n\{f(r)\}. \tag{11}$$

It is worth mentioning that by considering $f_R(r)=1$, edge effects are neglected and structures spatial extension is assumed to be infinite. By the aid of integral tables [35] for $\int_0^{+\infty} x\cos(\alpha x^2)J_n(bx)dx$ and $\int_0^{+\infty} x\sin(\alpha x^2)J_n(bx)dx$, it is a straightforward task to obtain

$$\mathcal{H}_n\{e^{i\alpha r^2}\} = \frac{b}{4}\left(\frac{\pi}{\alpha}\right)^{\frac{3}{2}} e^{-i\left(\frac{b^2}{8\alpha}-\frac{n\pi}{4}\right)}\times\left[J_{\frac{n+1}{2}}\left(\frac{b^2}{8\alpha}\right) + iJ_{\frac{n-1}{2}}\left(\frac{b^2}{8\alpha}\right)\right], \tag{12}$$

where $b = 2\pi\rho$. As the Hankel transform of zero order is same as the Fourier transform, we have

$$\mathcal{H}_0\{e^{i\alpha r^2}\} = \frac{i\pi}{\alpha} e^{\frac{-i\pi^2\rho^2}{\alpha}}. \tag{13}$$

Now, by replacing equations 12 and 13 in equation 10 we obtain

$$g(r,\theta) = e^{ikz}\times \left\{c_0 + \mathcal{R}e^{i\mathcal{R}^2}\textstyle\sum_{n=1}^{+\infty}\sqrt{\frac{\pi}{2}}(-i)^{\frac{n}{2}+1}(c_n e^{in\theta} + c_{-n}e^{-in\theta})\times\left[J_{\frac{n+1}{2}}(\mathcal{R}^2) + iJ_{\frac{n-1}{2}}(\mathcal{R}^2)\right]\right\}, \tag{14}$$

where $\mathcal{R}$ is a dimensionless quantity determined by $\mathcal{R} = \sqrt{\frac{\pi}{2\lambda z}}r$.

Equation 14 is the main result, and it shows the diffraction amplitude from radial structures.

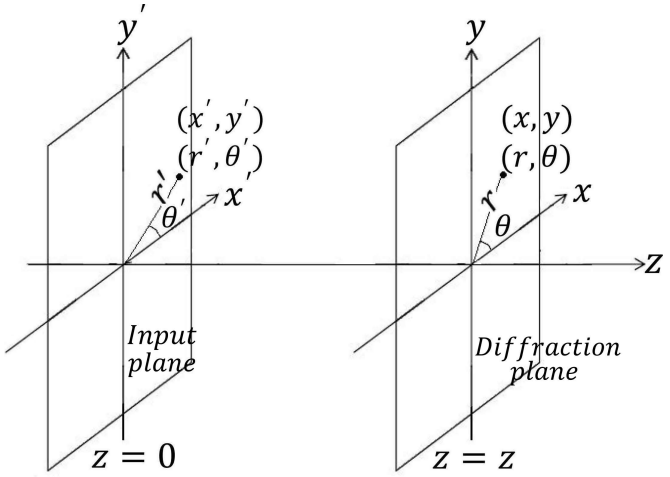

Fig. 1. Illustration of the diffraction geometry.

A. Plane wave diffraction from an amplitude radial grating with a sinusoidal transmission function

Now, we consider diffraction of a plane wave from an amplitude radial grating with a sinusoidal transmission function

$$t(\theta') = f_{\Theta}(\theta') = \tfrac{1}{2}[1+\cos(m\theta')] = \tfrac{1}{2} + \tfrac{1}{4}(e^{im\theta'} + e^{-im\theta'}), \quad (15)$$

where m is the number of spokes of the grating. A typical amplitude radial grating having sinusoidal transmission function with $m = 20$ is shown in Fig. 2(a).

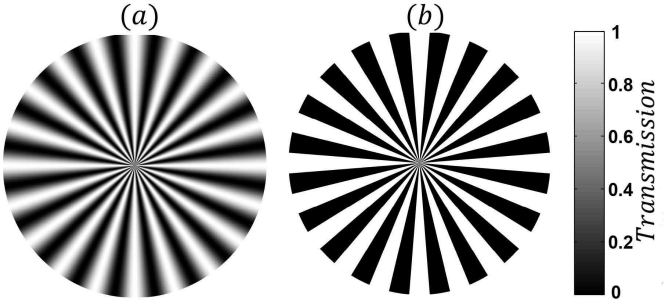

Fig. 2. Illustration of two typical amplitude radial gratings with spoke numbers of $m = 20$ having sinusoidal (a) and binary (b) transmission profiles.

By comparing equations 6 and 15, we have $c_0 = \frac{1}{2}$, $c_m = c_{-m} = \frac{1}{4}$, and $c_{n\neq m} = 0$, then from equation 14, the resulted complex amplitude of the light filed at a propagation distance z can be written by

$$g(r,\theta) = \tfrac{e^{ikz}}{2} \times \left\{1 + \mathcal{R}e^{i\mathcal{R}^2}\sqrt{\tfrac{\pi}{2}}(-i)^{\frac{m}{2}+1}\left[J_{\frac{m+1}{2}}(\mathcal{R}^2) + iJ_{\frac{m-1}{2}}(\mathcal{R}^2)\right]\cos(m\theta)\right\}. \quad (16)$$

Diffraction pattern at a given z can be calculated by $I(r,\theta) = g(r,\theta).g^*(r,\theta)$, where $*$ denotes complex conjugate.

Equation 16 specifies the diffraction amplitude of the radial grating in both near-field and far-field diffraction regimes and the geometric shadow. It shows the alternative change of the diffraction fringes in transverse plane as a function of radial coordinate, r, and as a function of propagation distance, z. As is apparent from equation 16, the diffraction pattern has a stable form respect to $\mathcal{R}$. In other words, for a constant value of $\mathcal{R}$, diffraction pattern remains unchanged, although the other two parameters, including propagation distance, z, and radial coordinate, r, change. For a given value of $\mathcal{R}$, as $r \propto \sqrt{z}\mathcal{R}$, the diffraction pattern scales by the square root of the propagation distance, $\sqrt{z}$. This means that, the trace of a given point on the intensity distribution for different propagation distances, is not a straight line. This feature is in consistent with the treatment of the conventional diffraction where angular form of the far-field diffraction pattern remains unchanged at different distances from the structure. It also is in consistent with the treatment of the conventional near-field diffraction where the diffraction pattern changes very rapidly by changing propagation distance.

For a given grating, diffraction pattern $I(r,\theta)$ at a given distance can be calculated by using equation 16. In Fig. 3 (a), calculated diffraction patterns for three sinusoidal amplitude radial gratings with spoke numbers of m=5, m=50, and $m = 75$, at a propagation distance of $z = 100\,cm$, are illustrated. For better illustration of the optical pattern formed at the transverse plane we project a sector of the second pattern from the polar coordinates to the Cartesian coordinates, Fig. 3 (b). As is apparent from Fig. 3 (a), for large values of radial distances a shadow image forms. Over an annular strip with a certain radius (or radial distance) as shown by the latter A in Fig. 3 (b), a sub-image or quarter-Talbot image of the structure with a number of radial fringes equal to $2m$ are formed. As spatial period in this radial distance is duplicated, in comparing to the conventional Talbot effect, we name the pattern over the defined annular strip as the first quarter-Talbot or sub-image of the corresponding annular strip of the grating with the same radius. In fact, in the vicinity and a bit larger than this radial distance, transition from the geometric shadow to near-field diffraction is occurred. We call this radial distance by r_{out}. Let us relate r_{out} to the propagation distance and spokes number. For this purpose, we need to recall definition of the quarter-Talbot distances for the conventional gratings. For a conventional grating with a period of p, its first quarter-Talbot image is formed at a propagation distance of $z = \frac{p^2}{2\lambda}$, where λ is the wavelength of the illuminating plane wave [36]. For a radial grating, over an annular strip with a radius of r_{out} the spatial period in the azimuthal direction is $p_{out} = \frac{2\pi r_{out}}{m}$ then at a given prorogation distance z, we have

$$r_{out} = \frac{m}{2\pi}\sqrt{2\lambda z}. \quad (17)$$

Other sub-images are formed at small radii that we call them higher-order sub-images. Radial location of the second sub-image is shown by C in Fig. 3 (b). Between the first and second sub-images' strips, as is shown by B in Fig. 3 (b), first half-Talbot image with a number of radial fringes equal to m and a half period azimuthal shift, is formed. First self-image or Talbot-image is formed between second and third sub-images, as is shown by D in Fig. 3 (b). By the same reasoning presented for the sub-images, radial location of the first Talbot-image can be determined from the Talbot distance of the conventional gratings $z_T = \frac{2p^2}{\lambda}$, by

$$r_{T1} = \frac{m}{2\pi}\sqrt{\lambda z/2}. \quad (18)$$

Let us clarify the matter with more details. Period of the structure is varying in the radial direction. But, over a given annular strip of the structure, as the radial coordinate and the period are almost constant, consequently self-images of this part of the structure forms at certain Talbot distances along z axis over an annular area with a same radial coordinate. Due to similarity of the radial grating diffraction pattern at the transverse plane, with the diffraction pattern of a conventional grating over a longitudinal plane that is known as the Talbot carpet, we name the observed optical pattern as "transverse Talbot carpet" or equally "radial Talbot carpet" and we call the area of formation of the sub- and self-images as the near-field regime.

Intensity profiles of the first and second sub-images and first half-Talbot and Talbot images for the grating introduced in Fig. 3 (b), are plotted in Fig. 3 (c). Also, along two radial lines passing from the extrema values of the shadow image, the intensity profiles are calculated and illustrated in Fig. 3(d).

A direct way for determining self- and sub-images' radii is the use of a recently proposed approach called "contrast variation method" [36]. It has been shown that, in the diffraction from a sinusoidal amplitude grating, contrast values for the self- and sub-images are maximum and minimum, respectively. Here, we define a visibility or equally a locally contrast value for the resulted pattern at a given radius by

$$\mathcal{V}(r) = \frac{I(r,\theta_{max}) - I(r,\theta_{min})}{I(r,\theta_{max}) + I(r,\theta_{min})}. \quad \textbf{(19)}$$

Now, radii of the self- and sub-images can be calculated respectively by determining maxima and minima of $\mathcal{V}(r)$ curve, as shown in Fig. 3 (e). We determined sub-images, half-Talbot, and Talbot images radii by using equation 19. Their values for the first sub- and Talbot-images are consistent with the calculated values obtained by equations 17 and 18, respectively.

In parallel to the analytical works, we have simulated the diffraction from the radial gratings using free space transfer function and Matlab programming for different propagation distances. In addition, with some amplitude radial gratings, with a diameter $3\,cm$ and different spokes, we have recorded diffraction patterns experimentally. In the experiment, a collimated wavefront of the second harmonic of an Nd:YAG diode pumped laser beam having wavelength of $\lambda = 532\,nm$ is propagated through the grating. The diffracted patterns at different distances from the grating are recorded by a camera (The Nikon D100). We record resulted patterns with two ways having a little difference in recording process. For recording the entire area of the diffraction patterns, we replace a diffuser on the path of the diffracted light beam at the desired propagation distances, then by the aid of imaging lens of the camera, resulted pattern on the diffuser is imaged on the active area of the camera with a magnification of about $1/2$. As the use of diffuser decline the quality of the images, in order to have high resolution diffraction patterns, we removed imaging lens of the camera, then we record diffraction patterns directly over the active area of the camera without any magnification in size. In this case, as the active image area of the camera is $23.4\,mm \times 15.6\,mm$, we lose some parts of the resulted images. For both of recording arrangements, the grating, the camera, and also the diffuser for the first case, are installed in the set-up in which their planes to be perpendicular to the propagation direction. The gratings' structures were constructed by a lithography method on transparent plates with a spatial resolution of 1200 dpi. Diameter of the constructed gratings was $30\,mm$. In the experiments, they are fully illuminated by a uniform laser beam.

In Fig. 4 , a typical experimentally recorded diffraction pattern for an amplitude radial grating with a sinusoidal profile and having 50 spokes at a distance equal to $100\,cm$ is shown. In the experiment, by removing imaging lens of the camera, the diffraction pattern is recorded directly on the active area of the camera with a real size of $23.4\,mm \times 15.6\,mm$.

For comparing results of the experimental works with simulated diffraction patterns, for different propagation distances from different radial gratings with a diameter of $3\,cm$, diffraction patterns are simulated. Also, for recording experimental patterns, as it mentioned above, by the aid of imaging lens of the camera, entire area of the produced diffraction patterns on the diffuser is imaged on the active area of the camera by a magnification of about $1/2$. Produced simulated diffraction patterns for three amplitude radial gratings with sinusoidal profiles and spokes numbers of 5, 50, and 75 at three different distances of $100\,cm$, $150\,cm$, and $200\,cm$ are shown with red color patterns in Fig. 5. For same gratings at same propagation distances, experimentally recorded diffraction patterns are shown by green color patterns in the same figure.

From the both simulated and experimentally recorded patterns of Fig. 5, it is apparent that, by decreasing radial distance, spacing between successive sub- and self-images decreases. Then, at a certain radial distance, near-field diffraction pattern completely disappears so that for each pattern an intensity patternless circular area around the optical axis appears.

For a complete realization of the diffraction from the radial gratings, we examined the cases of small propagation distances, which is in the conventional near-field regime. In Fig. 6, calculated and experimentally recorded diffraction patterns for an amplitude radial gratings with a sinusoidal profile and 50 spokes at three different distances of $20\,cm$, $30\,cm$, and $50\,cm$ almost in the conventional near-field distances are shown. For better illustration of the diffraction effect, only central parts of the patterns with a real size of $10\,mm \times 10\,mm$ are demonstrated. Here, in order to have high resolution images as much as possible, the experimental patterns are directly formed on the active area of the camera. By comparing pattern of Figs 5 and 6, we see that structure of the diffraction patterns at two ranges of the propagation distances are completely similar. It means that, in the diffraction from radial gratings, dividing the space only by the values of propagation distances into the conventional near-field and far-field regimes is meaningful and values of the radial distances should be taken into account.

As shown in Figs 3 - 6, over a given transverse Talbot plane, the near-field regime suddenly finishes at the border of the patternless area. In other words, the outer boundary of the patternless area is the inner boundary of the near-field regime that we call it r_{in}. Over the patternless area, the intensity value is very small and is constant in which it can be considered as the DC order of the far-field diffraction. Therefore, we call this area as the far-field regime.

As is apparent from Figs 3 , 5 and 6 and based on the theoretical predictions will be presented in the following, value of r_{in} depends on the propagation distance by $\sqrt{z}$. This means that, a given point on the inner boundary of the near-field regime, r_{in}, propagates on a curved line trajectory instead of a straight line path that occurs in the diffraction from conventional gratings at the far-field regime. By increasing the number of structure spokes, m, and value of z, radii of a given sub- or self-image ring increases.

Finally, unlike the conventional Talbot effect, here visibility of the self- or sub-images remains constant by propagation, see

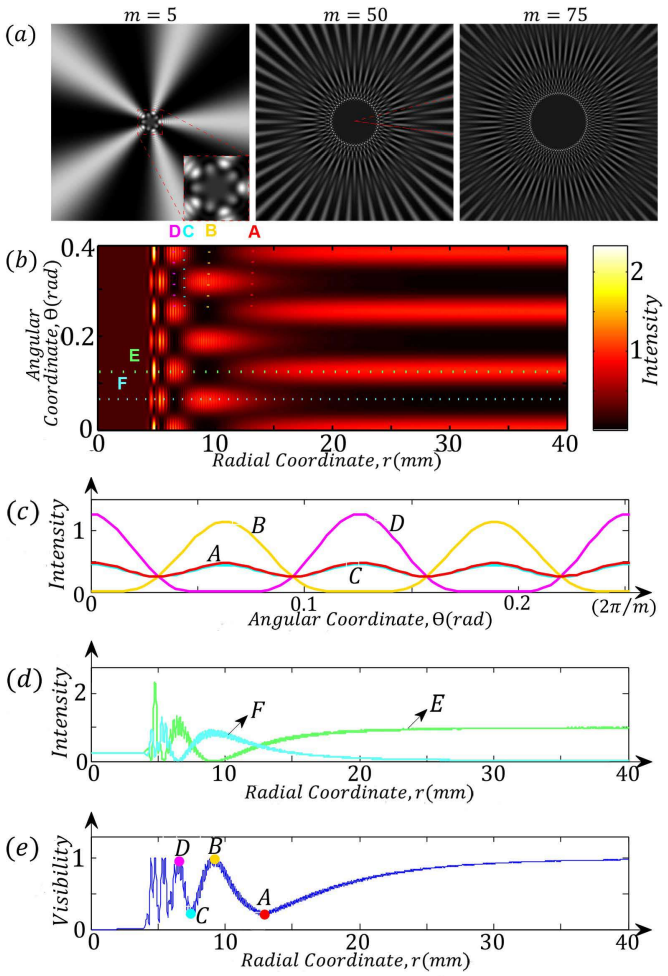

Fig. 3. Calculated diffraction pattern for three sinusoidal amplitude radial gratings with 5, 50, and 75 spokes at distance 100 cm from the gratings, (a), and projection of a sector of the theoretically produced transverse plane Talbot carpet from the polar coordinates to the Cartesian coordinates, (b). Calculated intensity profiles at radii equal to the locations of first and second sub-images (A and C plots) and first half-Talbot and Talbot-images (B and D plots), (c). Intensity profiles along two radial lines passing through locations of the extrema values of the shadow image, (d). Calculated visibility of the Talbot carpet as a function of radial distance from the optical axis, (e). Corresponding locations of the plots are shown in (b) by the same letters. Values of the intensities are normalized to the value of the incident beam's intensity (see also Visualization 1 and Visualization 2).

Visualizations 1 and 2. This means that at a given propagation distance the transverse Talbot carpet is observable. It needs to be mentioned that, this fact is valid for the radial gratings with infinite radial sizes.

It will be interesting realization of some of the above mentioned facts by some analytical predictions by considering some approximations on equation 16. For large values of r the Bessel function can be written as [33]

$$J_m(\mathcal{R}^2) \to \sqrt{\frac{2}{\pi\mathcal{R}^2}}\cos\left(\mathcal{R}^2 - \frac{m\pi}{2} - \frac{\pi}{4}\right). \tag{20}$$

By the use of the above approximation in equation 16, it reduces to

$$g(r,\theta) = \frac{e^{ikz}}{2}\{1+\cos(m\theta)\}, \tag{21}$$

where it produces desired geometric shadow.

In the vicinity of the optical axis, when r goes to zero, by using

$$J_m(\mathcal{R}^2) \to \frac{1}{\Gamma(m+1)}\left(\frac{\mathcal{R}^2}{2}\right)^m, \tag{22}$$

equation 16 reduces to

$$g(r,\theta) = \tfrac{e^{ikz}}{2} \times \left\{1+\sqrt{\pi}(-i)^{\frac{m}{2}+1}\mathcal{R}^m e^{i\mathcal{R}^2}\left[\frac{\mathcal{R}^2+i(m+1)}{2^{(\frac{m}{2})}(m+1)\Gamma(\frac{m+1}{2})}\right]\cos(m\theta)\right\}. \tag{23}$$

It means that in the vicinity of the optical axis, or equally at the far-field regime and for large values of m, the intensity gets a small and constant value, which was attributed to the DC term of the far-field diffraction.

Radius of the inner boundary of the near-field regime, r_{in}, can be determined both analytically and numerically as a function of both z and m by using equations 16 and 23. Nevertheless, analytically determining r_{in} by the aid of mentioned equations is not a straightforward task. For this reason, first we estimate the farthest distance of the near-field regime for a linear grating by considering the diffracted angles of the diffraction orders and by using geometric relations, then we generalize the resulted statement to the case of radial gratings. For a conventional grating with a period p and a lateral extension of d, at propagation distances larger than $\frac{pd}{2\lambda}$, different diffraction orders do not overlap and there is not any interference between them. As the near-field diffraction pattern is the interference of the different diffraction orders, therefore $z = \frac{pd}{2\lambda}$ can be assumed as the farthest border of the near-field regime for the conventional gratings. Now, for a radial grating with a spokes number of m, at a given radial of r we set r and $\frac{2\pi r}{m}$ as the lateral dimension and period of the grating, respectively, then we have

$$r_{in} = \sqrt{\frac{m\lambda z}{\pi}}. \tag{24}$$

By chasing the observed abrupt intensity changes on each sets of the calculated, simulated, or experimentally recorded patterns, above-introduced formula for the $r_{in}(z,m)$, can be verified. There is a good agreement between predicted values for r_{in} by equation 24 and those obtained for the radius of the patternless area of three sets of experimental, simulated, and calculated patterns. We see that r_{in}, unlike r_{out}, is proportional to $\sqrt{m}$ rather than m (see Figs 3 (a), 5 and 6).

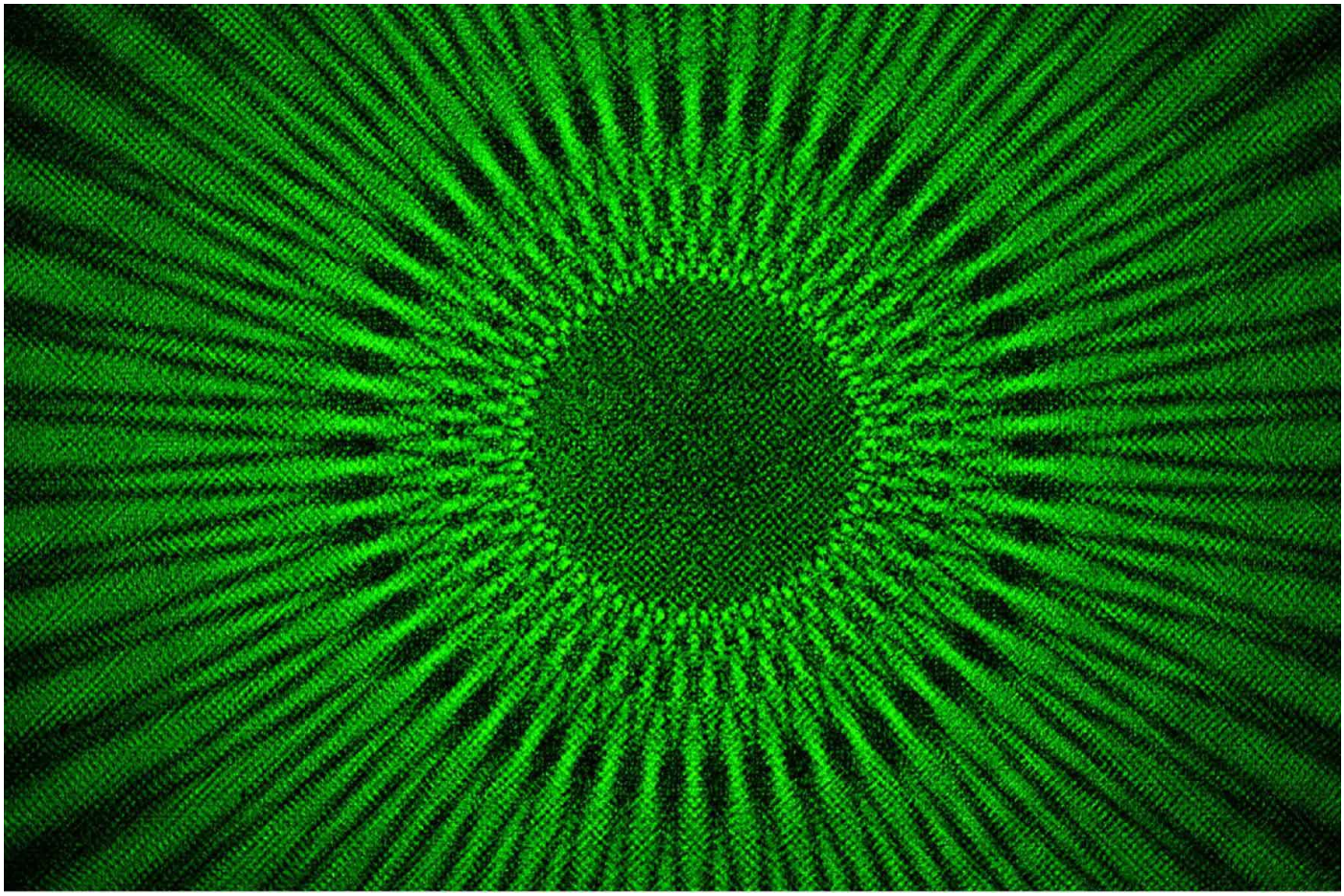

Fig. 4. An experimentally diffraction pattern from an amplitude radial grating with a sinusoidal profile and spokes number of $m = 50$ at a propagation distance equal to $100\,cm$ recorded directly on the active area of the camera. Real size of pattern is $23.4\,mm \times 15.6\,mm$ and wavelength of the impinging light was $532\,nm$.

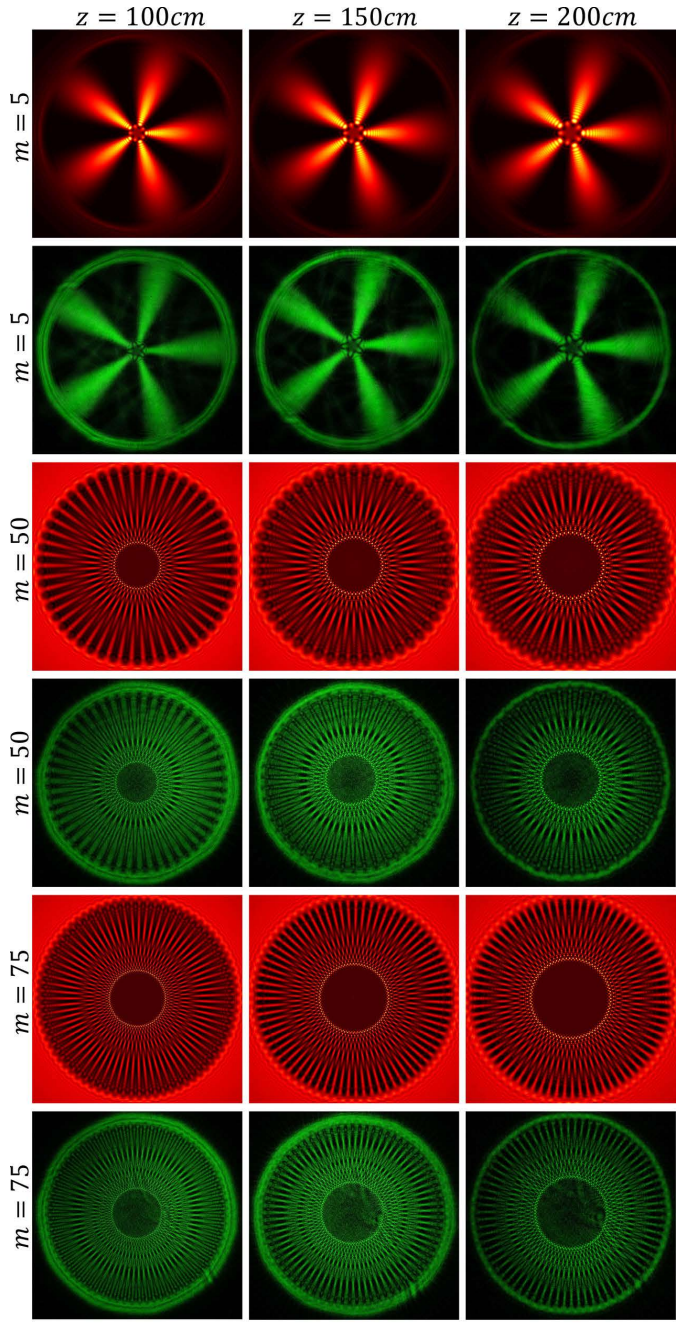

Fig. 5. Talbot carpets produced at the transverse planes by diffraction from amplitude radial gratings with sinusoidal profiles and spoke numbers of 5, 50, and 75 at different distances of 100 cm, 150 cm, and 200 cm from the gratings. Simulated and experimentally recorded patterns are illustrated by red and green colors, respectively. Real size of all patterns is $3\,cm \times 3\,cm$.

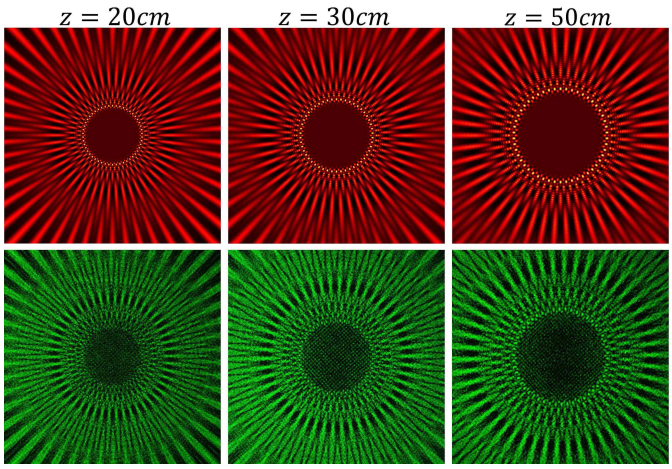

Fig. 6. Calculated (first row) and experimentally recorded (second row) diffraction patterns for a sinusoidal amplitude radial grating with 50 spokes at three different conventional near-field distances from the structure. Real size of all patterns is $10\,mm \times 10\,mm$.

Finally, we conclude that in the diffraction from radial gratings instead of conventional diffraction, the geometric shadow, and the near-field and far-field diffraction regimes are mixed at various propagation distances. In Fig. 7, for a given radial grating, boundaries between these regimes are demonstrated. Unlike the case of conventional diffraction that the diffraction regimes are divided by the flat borders, here the borders are parabolic surfaces.

For a radial grating with a finite size, further considerations are needed but it is beyond the aim of current work.

B. Diffraction from an amplitude radial grating with a binary profile

Now, we briefly investigate the case of an amplitude radial grating with a binary profile, Fig. 2 (b). Its transmission function can be written as

$$t(\theta') = \tfrac{1}{2}(1 + sgn\cos(m\theta')) \qquad (25)$$
$$= \tfrac{1}{2} + \textstyle\sum_{l=1}^{+\infty}(A_l e^{iml\theta'} + A_{-l}e^{-iml\theta'}),$$

where sng means signum function and Fourier coefficients are given by $A_{\pm l} = \frac{1}{2}\mathrm{sinc}(\frac{l\pi}{2})$, in which $A_0 = \frac{1}{2}$, $A_{\pm 1} = \frac{1}{\pi}$, $A_{\pm 2} = 0, \ldots$. As here again $f_R(r') = 1$, we have

$$f_\Theta(\theta') = \frac{1}{2} + \frac{1}{2}\sum_{l=1}^{+\infty}\mathrm{sinc}(\frac{l\pi}{2})(e^{iml\theta'} + e^{-iml\theta'}). \qquad (26)$$

By rewriting equation 26 in the form of equation 6, $c_0 = \frac{1}{2}$, $c_{n=ml} = c_{n=-ml} = \frac{1}{2}\mathrm{sinc}(\frac{l\pi}{2})$, $l = 1, 2, 3, \ldots$, are determined where all other coefficients are zero. Now, by use of the determined coefficients in equation 14, complex amplitude at z is given by

$$g(r,\theta) = \tfrac{e^{ikz}}{2} \times \qquad (27)$$
$$\left\{1 + \mathcal{R}e^{i\mathcal{R}^2}\textstyle\sum_{l=1}^{\infty} g_l\left[J_{\frac{ml+1}{2}}(\mathcal{R}^2) + iJ_{\frac{ml-1}{2}}(\mathcal{R}^2)\right]\cos(ml\theta)\right\},$$

where $g_l = \sqrt{2\pi}(-i)^{\frac{ml}{2}+1}\mathrm{sinc}(\frac{l\pi}{2})$. Similar to the case of the sinusoidal radial grating, in Fig. 8 , calculated diffraction patterns

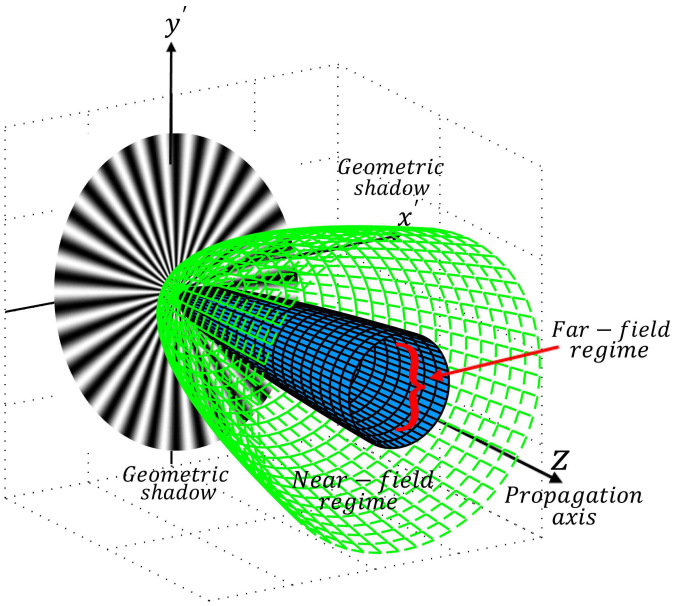

Fig. 7. Splitting of the space into geometric shadow and far-field and near-field diffraction regimes for a typical amplitude radial grating. Green surface splits the geometric shadow from the near-field diffraction regime and blue surface splits the near-field and far-field diffraction regimes from each other.

from three radial binary amplitude gratings with spoke numbers of 4, 50, and 75 for a propagation distance of 100 cm are shown.

The same as the case of the sinusoidal radial grating, in Fig. 9 a typical experimentally recorded diffraction pattern for an amplitude radial grating with a binary profile having spokes number of 50 at a propagation distance of 100 cm is also illustrated. Here again, in the experiment, by removing the imaging lens of the camera, the diffraction pattern is recorded directly on the sensitive area of the camera with a real size of 23.4 $mm \times 15.6\,mm$.

The simulation is done and the experimental diffraction pattern are taken for three radial binary amplitude gratings with spokes numbers of 4, 50, and 75 at four different distances of 100 cm, 150 cm, 200 cm, and 490 cm which are illustrated in Fig. 10 such as the cases of Fig. 5. Similar to the case of Fig. 6, in Fig. 11 the calculated and experimentally recorded diffraction patterns of a binary amplitude radial grating with 50 spokes at three almost conventional near-field distances are presented (see also Visualization 3).

By comparing patterns of Figs 3 – 6 with Figs 8 – 11 , we see that diffraction patterns of the amplitude gratings with sinusoidal and binary profiles are very similar. Meanwhile, the detailed investigation of the resulted patterns for the binary amplitude case is given up to the future studies.

As the subject of the diffraction from radial phase gratings is very close to the presented work, we have done both theoretical and experimental works in this regard. Results of that portion of work, have additional physical insight, and will be published as soon as possible.

4. CONCLUSION

In this work we have reported the first theoretical prediction and experimental observation of the Talbot carpet at any transverse plane in illuminating a radial grating by a spatially coherent light beam. We have shown that for the proposed structures, all

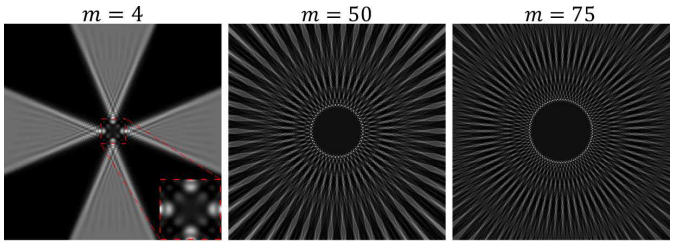

Fig. 8. Calculated diffraction patterns for three binary amplitude radial gratings with 4, 50, and 75 spokes at propagation distance of 100 cm.

three geometric shadow, and near-field and far-field diffraction patterns are observable at the planes parallel to the structure plane and continues distances from the structure. This achievement seems to have potential applications in the optical domain and can be extended to a wide range of wave physics phenomena in which the conventional Talbot effects were previously used.

In parallel to the current work, we have used the diffraction of a vortex beam from radial gratings for determining the topological charge of the vortex beam. Also, we proposed a simple method for optical switching by the aid of diffraction of vortex beams from radial gratings [37].

As a consequence of turning a conventional grating into a radial grating with a central singularity, the plane boundaries between the optical regimes have acquired curvature. The possibility of a connection with optical phenomena in a gravitational field is under investigation.

ACKNOWLEDGMENTS

Authors would like to thank Dr. Min Xiao for useful comments. This work was supported in part by the IASBS Research Council under grants No. G2016IASBS12632.

REFERENCES

1. L. Rayleigh, "XXV. On copying diffraction-gratings, and on some phenomena connected therewith," The London, Edinburgh, and Dublin Philosophical Magazine and Journal of Science 11.67 (1881): 196-205. Philos. Mag. 11, 196 (1881).
2. H. F. Talbot, "LXXVI. Facts relating to optical science. No. IV." The London and Edinburgh Philosophical Magazine and Journal of Science Philos. Mag. 9, 401 (1836).
3. M. K. Oberthaler, S. Bernet, E. M. Rasel, J. Schmiedmayer, and A. Zeilinger, "Inertial sensing with classical atomic beams," Phys. Rev. A 54, 3165 (1996).
4. J. Azana, and H. Guillet de Chatellus, "Angular Talbot effect," Phys. Rev. Lett. 112, 213902 (2014).
5. S. Rasouli, M. Dashti, and A. N. Ramaprakash, "An adjustable, high sensitivity, wide dynamic range two channel wave-front sensor based on moiré deflectometry," Opt. Express 18, 23906 (2010).
6. M. Yeganeh, S. Rasouli, M. Dashti, S. Slussarenko, E. Santamato, and E. Karimi, "Reconstructing the Poynting vector skew angle and wavefront of optical vortex beams via two-channel moiré deflectometery," Opt. Lett. 38, 887 (2013).
7. S. Rasouli and M. Taghi Tavassoly, "Application of the moiré deflectometry on divergent laser beam to the measurement of the angle of arrival fluctuations and the refractive index structure constant in the turbulent atmosphere," Opt. Lett. 33, 980 (2008).
8. M. Dashti and S. Rasouli, "Measurement and statistical analysis of the wavefront distortions induced by atmospheric turbulence using two-channel moiré deflectometry," J. Opt. 14, 095704 (2012).

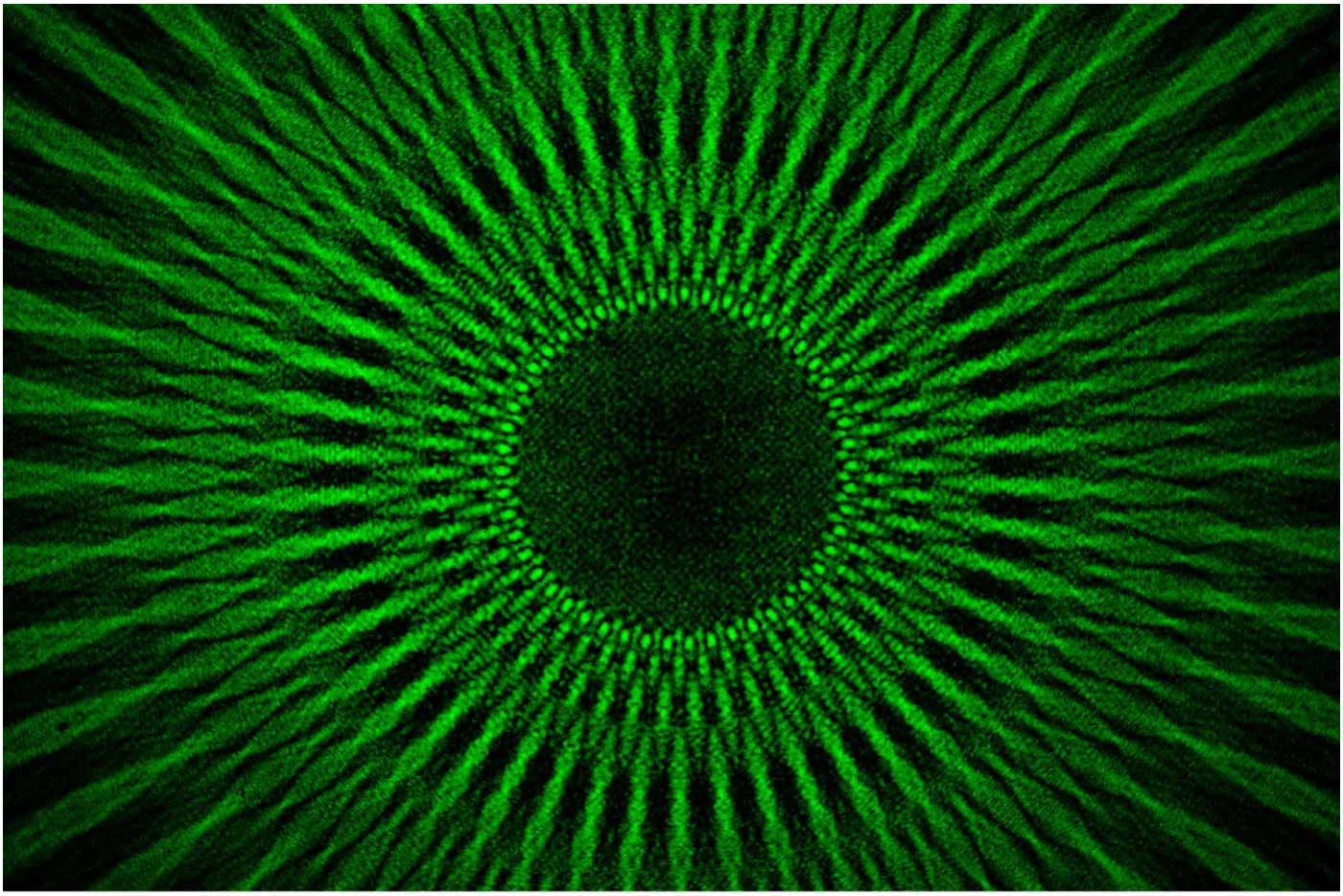

Fig. 9. An experimentally diffraction pattern from an amplitude radial grating with a binary profile and spokes number of $m = 50$ at a propagation distance of $100\,cm$. The pattern directly recorded on the sensitive area of the camera and its real size is $23.4\,mm \times 15.6\,mm$.

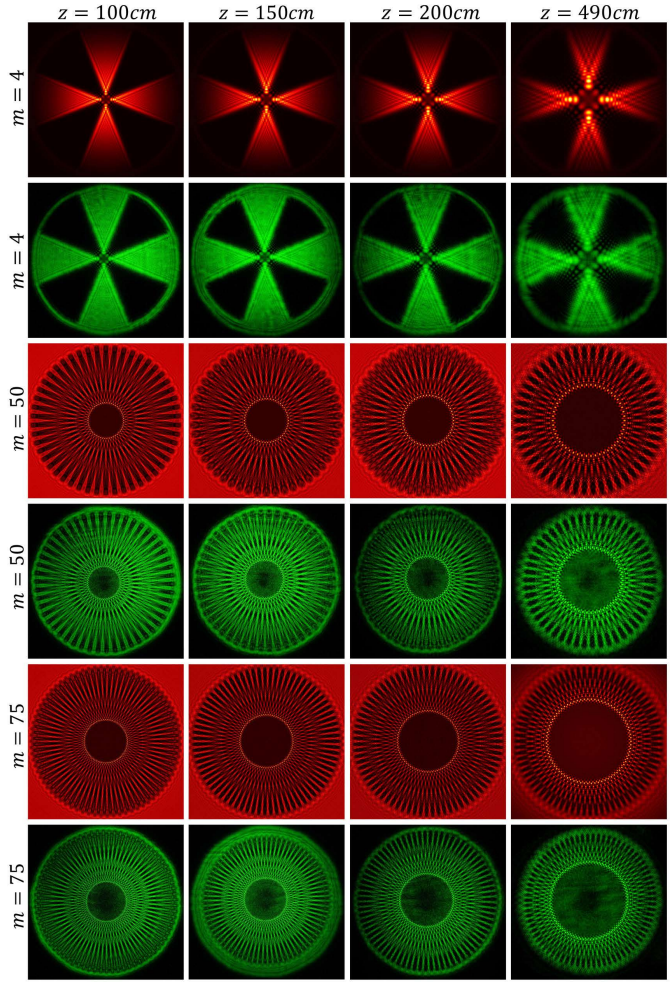

Fig. 10. Simulated and experimentally recorded diffraction patterns from three different radial binary amplitude gratings having binary profiles. The parameters of the gratings are same as the case of Fig. 5 and diffraction plane are considered at propagation distances of $100\,cm$, $150\,cm$, $200\,cm$, and $490\,cm$.

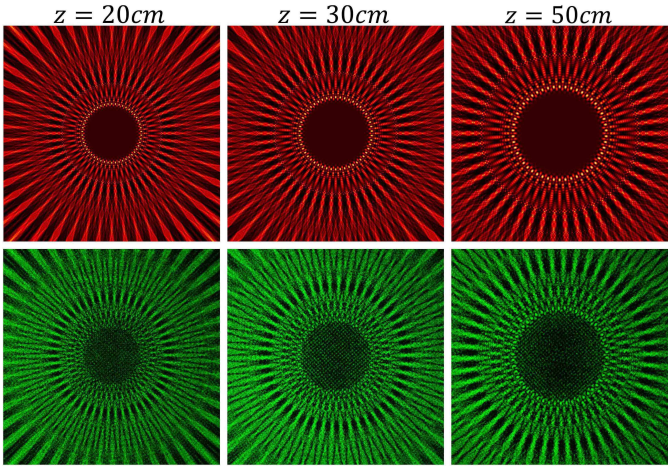

Fig. 11. Calculated (first row) and experimentally recorded (second row) diffraction patterns of a binary amplitude radial grating with 50 spokes at different almost conventional near-field distances (see also Visualization 3). Real size of all patterns is $10\,mm \times 10\,mm$.

9. F. X. D'Amato, E. T. Siebert, and C. Roychoudhuri, "Coherent operation of an array of diode lasers using a spatial filter in a Talbot cavity," Appl. Phy. Lett. 55, 816 (1989).
10. J. Wen, Y. Zhang, and M. Xiao, "The Talbot effect: recent advances in classical optics, nonlinear optics, and quantum optics," Adv. Opt. Photonics 5, 83 (2013).
11. Y. Zhang, J. Wen, S. N. Zhu, and M. Xiao, "Nonlinear Talbot effect," Phys. Rev. Lett. 104, 183901 (2010).
12. B. J. McMorran, and A. D. Cronin, "An electron Talbot interferometer," New J. Phys. 11, 033021 (2009).
13. J. A. Salas, K. Varga, J. A. Yan, and K. H. Bevan, "Electron Talbot effect on graphene," Phys. Rev. B, 93, 104305 (2016).
14. A. Momose, S. Kawamoto, I. Koyama, Y. Hamaishi, K. Takai, and Y. Suzuki, "Demonstration of X-ray Talbot interferometry," Jpn. J. Appl. Phys 42, L866 (2003).
15. M. R. Dennis, N. I. Zheludev, and F. J. G. de Abajo, "The plasmon Talbot effect," Opt. Express 15, 9692 (2007).
16. T. Gao, et al. "Talbot Effect for Exciton Polaritons," Phys. Rev. Lett. 117, 097403 (2016).
17. S. Mansfeld, J. Topp, K. Martens, J. N. Toedt, W. Hansen, D. Heitmann, and S. Mendach, "Spin wave diffraction and perfect imaging of a grating," Phys. Rev. Lett. 108, 047204 (2012).
18. X.B. Song, H.B. Wang, J. Xiong, K. Wang, X. Zhang, K.H. Luo, and L.A. Wu, "Experimental observation of quantum Talbot effects," Phys. Rev. Lett. 107, 033902 (2011).
19. S. Deachapunya, S. Srisuphaphon, P. Panthong, T. Photia, K. Boonkham, and S. Chiangga, "Realization of the single photon Talbot effect with a spatial light modulator," Opt. express 24, 20029–20035 (2016).
20. H. Guillet de Chatellus, E. Lacot, W. Glastre, O. Jacquin, and O. Hugon, "Theory of Talbot lasers," Phys. Rev. A 88, 033828 (2013).
21. R. Iwanow, D. A. May-Arrioja, D. N. Christodoulides, G. I. Stegeman, Y. Min, and W. Sohler, "Discrete Talbot effect in waveguide arrays," Phys. Rev. Lett. 95, 053902 (2005).
22. M. S. Chapman, C. R. Ekstrom, T. D. Hammond, J. Schmiedmayer, B. E. Tannian, S. Wehinger, and D. E. Pritchard, "Near-field imaging of atom diffraction gratings: The atomic Talbot effect," Phys. Rev. A 51, R14 (1995).
23. B. Brezger, L. Hackermüller, S. Uttenthaler, J. Petschinka, M. Arndt, and A. Zeilinger, "Matter-wave interferometer for large molecules," Phys. Rev. Lett. 88, 100404 (2002).
24. L. Deng, E. W. Hagley, J. Denschlag, J. E. Simsarian, M. Edwards, C. W. Clark, K. Helmerson, S. L. Rolston, and W. D. Phillips, "Temporal, matter-wave-dispersion Talbot effect," Phys. Rev. Lett. 83, 5407 (1999).
25. S. Aghion, et al. "A moiré deflectometer for antimatter," Nat. Commun. 5, 4538 (2014).
26. M. Berry, I. Marzoli, and W. Schleich, "Quantum carpets, carpets of light," Phys. World 14, 39 (2001).
27. W. B. Case, M. Tomandl, S. Deachapunya, and M. Arndt, "Realization of optical carpets in the Talbot and Talbot–Lau configurations," Opt. Express 17, 20966–20974 (2009).
28. S. Rasouli and D. Hebri, "Contrast enhanced quarter-Talbot images", J. Opt. Soc. Am. A (manuscript accepted), 2017.
29. P. Szwaykowski, "Self-imaging in polar coordinates," J. Opt. Soc. Am. A 5, 185–191 (1988).
30. J. Alonso and E. Bernabeu, "Spatial evolution of Gaussian beams diffracted by radial gratings," Opt. Comm. 98, 323–330 (1993).
31. J. Alonso and E. Bernabeu, "Use of effective focal lengths to describe laser-beam evolution after diffraction in radial gratings," J. Opt. Soc. Am. A 10, 1963–1970 (1993).
32. B. E. A. Saleh, M. C. Teich, and B. E. Saleh, Fundamentals of photonics, Vol. 22. (New York: Wiley, 1991).
33. G. B. Arfken, Mathematical Methods for Physicists, 3nd (Academic Press, 1985).
34. J. W. Goodman, Introduction to Fourier Optics, 2nd ed (Singapore: Mcgraw-Hill, 1996).
35. A Jeffrey and D. Zwillinger, eds. Table of integrals, series, and products

(Academic Press, 2007).
36. S. Rasouli, D. Hebri, and A. M. Khazaei, "Investigation of various behaviors of near- and far-field diffractions from multiplicatively separable structures in the x and y directions, and a detailed study of the near-field diffraction patterns of 2D multiplicatively separable periodic structures using the contrast variation method," J. Opt. 19, 095601 (2017).
37. S. Rasouli, Department of Physics, IASBS, Zanjan, Iran, and D. Hebri and M. Yeganeh are preparing a manuscript to be called "Determining the topological charge of vortex beams and an optical switch by the aid of diffraction of vortex beams from radial gratings."